IEEE Access
Multidisciplinary ⋮ Rapid Review ⋮ Open Access Journal

Received 4 October 2024, accepted 17 October 2024, date of publication 23 October 2024, date of current version 31 October 2024.

Digital Object Identifier 10.1109/ACCESS.2024.3485135

RESEARCH ARTICLE

Phase Offset Aided Index Modulation for UCA-Based OAM Communication

HYE YEONG LEE[1], MAN HEE LEE[2], (Member, IEEE), AND SOO YOUNG SHIN[3], (Senior Member, IEEE)

[1]ICT Convergence Research Center, WENS Laboratory, Kumoh National Institute of Technology, Gumi 39177, South Korea
[2]WENS Laboratory, Kumoh National Institute of Technology, Gumi 39177, South Korea
[3]Department of IT Convergence Engineering, WENS Laboratory, Kumoh National Institute of Technology, Gumi 39177, South Korea

Corresponding authors: Soo Young Shin (wdragon@kumoh.ac.kr) and Man Hee Lee (fordmore@kumoh.ac.kr)

This work was supported in part by the Ministry of Science and ICT (MSIT), South Korea, under the Information Technology Research Center (ITRC) Support Program (50%) supervised by the Institute for Information & Communications Technology Planning & Evaluation (IITP) under Grant IITP-2024-RS-2024-00437190; and in part by the Basic Science Research Program through the National Research Foundation of Korea (NRF) funded by the Ministry of Education (50%) under Grant 2022R1I1A1A01066178.

ABSTRACT In this paper, a novel phase offset (PO)-aided index modulation (IM) for orbital angular momentum (OAM) communication, called OAM-PO-IM, is proposed to enhance capacity. The proposed system conveys two types of index information including an active mode combination (AMC) and misalignment of PO states. This method leverages the PO state induced by the selective activation of antenna elements within a uniform circular array (UCA). Specifically, a UCA is divided into multiple uniform circular subarrays (UCSAs) in the transmitter, and additional index bits are allocated according to the activation state of the UCSAs. In addition, the modified Bessel function (MBF) of the first kind is used to derive the channel model to allow a straightforward determination of the optimal AMC for the OAM-IM system. To detect index and symbol bits, the receiver provides a maximum likelihood (ML) detector and a new low-complexity ML detector using the log-likelihood ratio (LLR). The effectiveness of the proposed OAM-PO-IM is verified through comprehensive simulations that benchmark its performance against the existing OAM and OAM-IM in terms of sum capacity, bit error rate (BER), and energy efficiency. Compared with the OAM-IM, the proposed OAM-PO-IM provides a capacity gain of additional $\log_2 G$ bps/Hz, where G denotes the number of UCSA. Furthermore, this scheme improves the gain by approximately 1 dB at a BER of 10^{-4} for active mode $L_A = 2$ at 6 bps/Hz.

INDEX TERMS 6G, index modulation (IM), orbital angular momentum (OAM), uniform circular array (UCA), phase offset (PO).

I. INTRODUCTION

Recently orbital angular momentum (OAM) has attracted interest in radio communication to enhance spectral efficiency (SE). The vortex electromagnetic (EM) waves of OAM are generated by twisting or rotating the waves around the axis of propagation, which is known as OAM mode. Theoretically, OAM vortex waves with the same frequency can exist in an infinite number of inherently orthogonal modes. Mode division multiplexing (MDM) using OAM has particularly attracted research interest because of its potential to enhance SE. This technique involves multiplexing signals by using a set of orthogonal OAM modes at the same frequency [1], [2]. In 2021, NTT demonstrated an OAM multiplexing communication system achieving data rates over 200 Gbit/s in the 28 GHz band [3]. Additionally, OAM multiplexing has been demonstrated in the sub-THz and THz bands [4], [5].

Specific antenna types are required to generate a vortex beam for OAM communication, such as spiral phase plates, helicoidal parabolic antennas, uniform circular arrays (UCA), and metasurfaces. The UCA antenna structure is widely

The associate editor coordinating the review of this manuscript and approving it for publication was Yafei Hou.

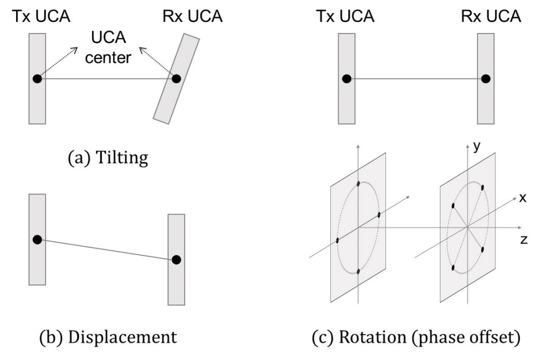

FIGURE 1. Misalignment in Tx-Rx UCA (a) Tilting (b) Displacement (c) Rotation (phase offset).

used to generate unique OAM modes due to its simple structure and compatibility with antenna arrays at 4G/5G/6G base stations [6], [7]. However, UCA-based OAM still presents technical challenges, such as misalignment and beam divergence.

One of the challenges in UCA-based OAM communication is the misalignment occurring between the transmitter (Tx) and receiver (Rx) UCA antennas. Generally, misalignment of OAM communication is categorized into three types: tilting, displacement, and rotation [8], [9], as shown in Fig. 1. It can be seen from the figure that Tx and Rx UCA are located in the xy-plane and the beam axis is the z-axis. The tilting misalignment was characterized by the Tx and Rx UCA planes not being parallel, exhibiting an oblique angle between transceiver UCAs. However, displacement and rotation misalignment were observed when the Tx and Rx UCA planes were parallel. A displacement misalignment is identified when the center of the Rx UCA does not aligned with that of the transmitted beam. Rotation misalignment, referred to as phase offset (PO) in this paper, is observed when one UCA rotates around the beam axis, while the Tx and Rx UCAs retain parallel planes and aligned center. Consequently, tilting and displacement misalignment lead to notable performance degradation by distorting the OAM beams, resulting in inter-mode interference and mode turbulence [8]. In contrast, PO misalignment predominantly influences the phase front while maintaining orthogonality among the different modes [9].

Although OAM theoretically supports infinite orthogonal modes, practical limitations affect the mode usability. Specifically, high-order OAM mode beams tend to diverge and suffer significant attenuation in free space [10]. To mitigate the impact of beam divergence, the use of low-order OAM modes rather than high-order modes is beneficial for achieving higher SE. Therefore, in the OAM-MDM system, optimizing mode combinations based on the antenna structure to mitigate beam divergence and maximize capacity has become a crucial topic [11].

To further improve the SE of OAM, integrated index modulation (IM) with the OAM-MDM scheme was first proposed in [12] by activating several OAM modes, namely OAM-IM. OAM-IM achieved better error performance than OAM-MDM with similar detection complexity by employing low-complexity detection. The study in [13] expanded the OAM-IM methodology by adjusting different modulation orders for each activated OAM mode, with higher SE. Further advancing the field, [14] introduced two robust detectors for OAM-IM under conditions of tilting misalignment, employing both the angle of arrival (AoA) and deep learning (DL) techniques. However, these studies have not yet investigated the optimal mode combination to maximize the capacity of an OAM-IM system.

In [15], OAM spatial modulation (OAM-SM) was introduced for a millimeter-wave communication system, leveraging the spatial distribution characteristics of OAM beams. To generate beams with different OAM modes, antennas configured in a uniform linear array were equipped with traveling-wave-ring resonators. Depending on the antenna structure, the OAM-SM system can transmit signals through a single OAM mode by selecting one of the transmission antennas. However, this approach did not consider mode multiplexing or OAM-IM integration.

Motivated by the above discussion, this paper introduces a novel OAM-IM technique that utilizes both an active mode combination (AMC) and an activation pattern of a subset of antenna elements in the UCA structure. Specifically, the activation of these subset antenna elements leads to a misalignment of the PO state, which we refer to as the OAM-PO-IM system. Inspired by grouping generalized spatial modulation (gGSM) [16], [17], the proposed system is equipped with a transmitter with a single UCA antenna divided into numerous uniform circular subarrays (UCSA). Correspondingly, the receiver employs a singular UCA antenna that embodies the same antenna configuration as the Tx UCSA. The transceiver can adjust the alignment or misalignment state depending on the active UCSA, thereby allowing the allocation of additional index bits using the IM technique. Consequently, OAM-PO-IM offers an efficient approach for improving the capacity with fewer active RF chains.

The main contributions of the paper are summarized as follows.

- In this paper, a new OAM-IM scheme is proposed using UCSA activation as the PO state difference, called OAM-PO-IM.
- An effective AMC selection scheme is introduced by deriving an OAM channel model using a modified Bessel function (MBF). This approach employs a priority-based methodology for the lower-order OAM modes.
- Two detectors for OAM-PO-IM are proposed as a maximum likelihood (ML) detector and a log-likelihood ratio (LLR) based low-complexity ML detector.

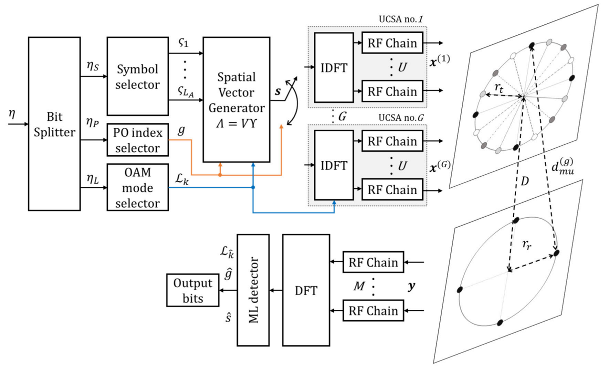

FIGURE 2. Transceiver system for the proposed OAM-PO-IM.

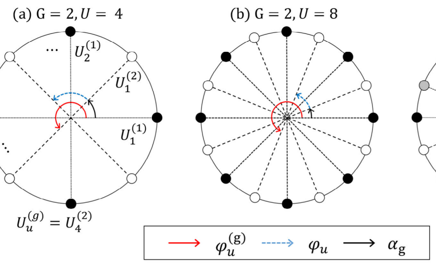

FIGURE 3. Azimuth angle of the UCSA in a Tx UCA (a) $G = 2, U = 4$ (b) $G = 2, U = 8$ (c) $G = 4, U = 4$.

- The proposed system is analyzed and simulated in terms of the sum capacity bounds by mutual information (MI), upper bound of the bit error rate (BER), and energy efficiency compared to the existing OAM and OAM-IM schemes.

The remainder of this paper is organized as follows. Section II describes the OAM-PO-IM system and channel model. Section III presents an effective AMC selection scheme for the OAM-IM. Section IV presents the performance analysis in terms of sum capacity, BER, complexity, and energy efficiency. The numerical results are presented in Section V. Finally, the conclusions are presented in Section VI.

II. SYSTEM MODEL

The proposed system employs the UCSA in the MDM-based OAM-IM system investigated in [12], as shown in Fig. 2. In the OAM-IM system, more than one OAM mode L_A is activated simultaneously, and the kth AMC can be denoted as $\mathcal{L}_k = \{l_1, \cdots, l_{L_A}\}$. Moreover, the active L_A OAM modes transmit different data symbols. Consequently, the L_A modes transmit modulated signals through the selected UCSA. The total number of antenna elements for the Tx and Rx UCA are N and M, respectively. A single UCA is composed of G UCSA groups, with each UCSA comprising U antenna elements, where $N = GU$. It is assumed $G \geq 2$ to incorporate the principle of IM. In addition,

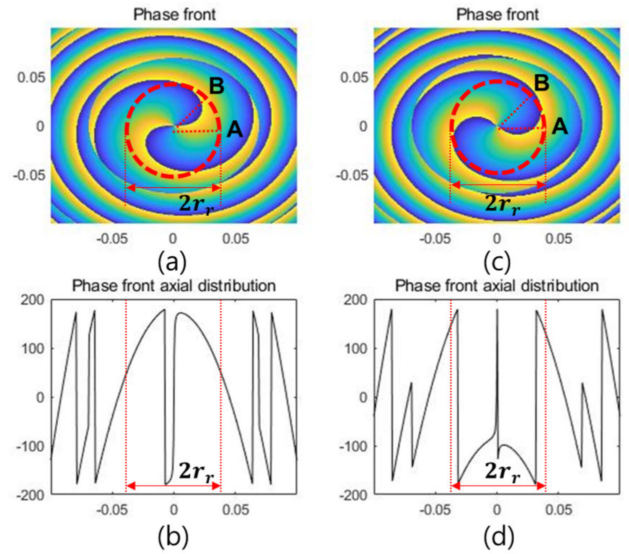

FIGURE 4. Difference in the shape and distribution of the phase front with OAM mode $l = 2$ (a),(b) align case (c),(d) phase offset misalignment case, where $2r_r$ is diameter of Rx UCA, the point A and B are the antenna elements forming the minimum spacing of Rx UCA.

the number of antenna elements is matched between the Tx and Rx UCA to maximize channel capacity. Therefore, in this paper, it is assumed that Tx UCSA and Rx UCA have an equal number of antenna elements as $U = M$. The bit per channel use (bpcu) of the proposed system can be written as

$$\eta = \underbrace{L_A \log_2 \mathcal{M}}_{\text{symbol bits}, \eta_S} + \underbrace{\lfloor \log_2 G \rfloor + \lfloor \log_2 C(L, L_A) \rfloor}_{\text{index bits}, \eta_P + \eta_L}, \quad (1)$$

where $\lfloor \cdot \rfloor$ represents the floor function and $C(\cdot, \cdot)$ is the binomial coefficient. $\mathcal{M}$-ary phase shift keying (PSK) was considered for modulation. L is the total number of OAM modes in the given UCSA. Generally, the available OAM mode can be represented as $\lfloor \frac{-U+2}{2} \rfloor \leq l \leq \lfloor \frac{U}{2} \rfloor$ where the maximum number of OAM modes is U Tx antenna elements [18]. Although OAM mode 0 is not a vortex beam, earlier research on OAM included it by placing an extra antenna in the center of the UCA. However, the OAM mode 0 state is excluded in our proposed PO-IM scheme since the PO state characteristic only occurs in vortex beams. Therefore, the available OAM mode in this paper can be denoted as $L = \left[\lfloor \frac{-U+1}{2} \rfloor, \cdots, \lfloor \frac{U}{2} \rfloor \right]$ and $0 \notin L$.

According to the properties of the vortex beam, the OAM beam is generated by the phase-shifted signal as the helical phase term $e^{jl\varphi}$, where l is the index of the OAM mode and φ is the azimuth angle. In the basic UCA structure, the nth and the mth azimuth angle of the Tx and Rx UCA denote $\varphi_n = \frac{2\pi(n-1)}{N} + \alpha_0$ and $\varphi_m = \frac{2\pi(m-1)}{M} + \theta_0$, respectively. Here, a_0 and θ_0 are the initial angles of the first element position in the Tx and Rx UCA, respectively. For simplicity, a_0 and θ_0 were set to zero.

A. PO STATE GENERATION

To generate the PO states, the Tx UCA is divided into multiple UCSAs. Each subset of active antenna elements is uniformly distributed in a UCSA structure adhering to the inherent UCA configuration. To maintain a practical and effective design, we assumed that the minimum number of elements per UCSA to be $\min(U) = 4$. Furthermore, the maximum number of groups G was determined to ensure that the spacing between adjacent elements within each UCSA, $d_{u,u+1}$ remained larger than $\lambda/2$, where λ is the wavelength of the carrier frequency. This spacing criterion is critical to avoid mutual coupling effects that can degrade system performance in antenna design [11]. With the PO state set, the azimuth angle for the uth elements corresponding to the gth UCSA can be expressed as

$$\varphi_u^{(g)} = \varphi_u + \alpha_g = \frac{2\pi(u-1)}{U} + \frac{2\pi(g-1)}{N}, \tag{2}$$

where φ_u denotes the azimuth angle of the uth element of the Tx UCSA. α_g represents the initial angle of the first element corresponding to the gth UCSA. Fig. 3 shows an example of the azimuth angle in the Tx UCA structure of the proposed system. Each UCSA consists of elements of the same color in the figure. For example, as illustrated in Fig. 3.(a), a Tx UCA can be divided into two UCSAs ($G = 2$) consisting of $U = 4$ elements. In this case, the initial angle of each UCSA is denoted by $\alpha_1 = 0°$ and $\alpha_2 = 45°$. Fig. 3.(b) and (c) represent the Tx UCA with $N = 16$ elements decomposed into $G = 2, 4$, respectively.

The feasibility of the PO state is expressed in terms of the EM waves, as shown in Fig. 4. It can be seen from the figure that the phase front shape and distribution for OAM mode $l = 2$ are different with respect to align and PO misalignment cases. Figs. 4.(a) and (b) illustrate the align case, whereas (c) and (d) represent the PO misalignment case, respectively. The phase front shapes are shown in Figs. 4.(a) and (c), where the dashed circle represents the Rx antenna with a diameter of $2r_r$, and points A and B denote the antenna elements forming the minimum spacing of the Rx antenna. Differences depending on the PO state can be observed through the distribution along the phase front axis, as depicted in Figs. 4.(b) and (d). As shown in the figure, the PO state generates unique phase fronts. Hence, this characteristic of the PO state is proposed to be utilized as an index resource in this paper.

To verify with the formula, the modes can be demultiplexed by applying a phase term $e^{-j\varphi_m}$ on the receiver side [19]. The sum of the received azimuth phase of the mth element at the Rx UCA, corresponding to the transmitted l mode and the expected $\hat{l}$ mode, can be represented as

$$\sum_{m=1}^{M} \exp\left[j\left(\frac{2\pi(u-1)}{U} + \alpha_g\right)l\right] \exp\left[-j\frac{2\pi(m-1)}{M}\hat{l}\right]$$
$$= \sum_{m=1}^{M} \exp\left[j\frac{2\pi(m-1)}{M}\left(l-\hat{l}\right) + j\alpha_g l\right]$$
$$= \begin{cases} 0, & l \neq \hat{l}; \\ M, & l = \hat{l}, \quad \text{w/o PO;} \\ M\exp(j\alpha_g l), & l = \hat{l}, \quad \text{w/ PO,} \end{cases} \tag{3}$$

Note that the sum of the received azimuth phases can be zero when different OAM modes are used. However, different PO states for the same modes have distinct phase sums. According to (3), the PO state can be distinguished in the EM waves. Moreover, the generation of dual and multimodes has been verified in previous studies [6], [20]. In the next section, we introduce the channel and signal model incorporating the proposed PO state, considering a radio line-of-sight (LOS) OAM communication system.

B. CHANNEL AND SIGNAL MODEL

By applying the free space LoS channel model [2], the channel between the uth antenna element corresponding to the gth UCSA and the mth Rx antenna element can be expressed as

$$h_{mu}^{(g)} = \frac{\beta}{2k_0 d_{mu}^{(g)}} e^{-jk_0 d_{mu}^{(g)}}, \tag{4}$$

where λ is the wavelength of the carrier frequency, $k_0 = 2\pi/\lambda$ is the propagation constant, β is a constant related to antenna gains. The distance from the uth element in the gth Tx UCSA to the mth Rx UCA element is represented as

$$d_{mu}^{(g)} = \sqrt{D^2 + r_t^2 + r_r^2 - 2r_t r_r \cos\left(\varphi_m - \varphi_u^{(g)}\right)}$$
$$\overset{(a)}{\approx} \sqrt{D^2 + r_t^2 + r_r^2} - \frac{r_t r_r \cos\left(\varphi_m - \varphi_u^{(g)}\right)}{\sqrt{D^2 + r_t^2 + r_r^2}}, \tag{5}$$

where D is the transmission distance and r_t and r_r are the radii of the Tx and Rx UCA, respectively. (a) follows by defining $\sqrt{1-2x} \approx 1 - x$ based on the Taylor series expansion and $r_t, r_r \ll D$ [21].

By substituting (5) into (4), the proposed channel between the uth Tx and the mth Rx antenna element corresponding to the gth Tx UCSA can be rewritten as

$$h_{mu}^{(g)} \approx \frac{\beta e^{-jk_0\sqrt{D^2+r_t^2+r_r^2}}}{2k_0\sqrt{D^2+r_t^2+r_r^2}} e^{jk_0 \frac{r_t r_r \cos\left(\varphi_m - \varphi_u^{(g)}\right)}{\sqrt{D^2+r_t^2+r_r^2}}}. \tag{6}$$

The same input signal s_l is fed by the array elements in the UCA with different phase shifts $e^{j\varphi_u^l}$ corresponding to each element [21]. In the proposed system, the same input signal was applied to each Tx UCSA. The transmit signal with the MDM corresponding to the uth element on the gth Tx UCSA is given by

$$x_u^{(g)} = \sum_{l\in\mathcal{L}_k} x_{l,u}^{(g)} = \sum_{l\in\mathcal{L}_k} \frac{1}{\sqrt{U}} s_l e^{j\varphi_u^{(g)} l}, \tag{7}$$

where $x_{l,u}^{(g)}$ denotes the lth mode signal to the uth element on the gth Tx UCSA. $\mathcal{L}_k = \{k_1, k_2, \ldots, k_{L_A}\}$ is the set of active OAM modes for the kth AMC of OAM-IM, where $k \in \{1, 2, \ldots, p_c\}$ and $p_c = 2^{\lfloor \log_2 C(L,L_A) \rfloor}$ is the total number of AMC [12]. Using (7), the transmit signal vector corresponding to the gth Tx UCSA can be written as

$$\boldsymbol{x} = \boldsymbol{W}^H \boldsymbol{s}, \tag{8}$$

where $\boldsymbol{x} \in \mathbb{C}^{N\times 1}$ is defined as the transmit signal vector consisting of all Tx UCSA signals $\boldsymbol{x} = \left[\boldsymbol{x}^{(1)}\boldsymbol{x}^{(2)}\cdots\boldsymbol{x}^{(G)}\right]^T$. The signal vector of the gth Tx UCSA is $\boldsymbol{x}^{(g)} = \left[x_u^{(g)}\right]_{U\times 1}$. $\boldsymbol{W}^H = \mathrm{diag}\left[\boldsymbol{W}_{(1)}^H\boldsymbol{W}_{(2)}^H\cdots\boldsymbol{W}_{(G)}^H\right]$ is a $N \times N$ diagonal matrix, where $\boldsymbol{W}_{(g)}^H$ is an $U \times U$ inverse discrete Fourier transform (IDFT) matrix corresponding to the gth Tx UCSA. $\boldsymbol{s}$ is N-dimensional transmitted signal vector.

The transmitted signal vector $\boldsymbol{s}$ consists of the active symbol vector ς_l and some zero values owing to IM as the AMC and UCSA pattern based on the look-up table (LUT). Thus, $\boldsymbol{s}$ can be rewritten by the AMC matrix $\boldsymbol{\Upsilon}_k \in \mathbb{C}^{L\times L_A}, k = \{1,\cdots,2^{\eta_L}\}$ and the active UCSA pattern matrix $\boldsymbol{V}_g \in \mathbb{C}^{N\times L}, g = \{1,\cdots,2^{\eta_P}\}$. Consequently, the fth proposed index matrix can be denoted as $\boldsymbol{\Lambda}_f = \boldsymbol{V}\boldsymbol{\Upsilon} \in \mathbb{C}^{N\times L_A}, f = \{1,\cdots,F\}$, and $F = 2^{\eta_P+\eta_L}$, which consists of L_A non-zero elements and $L_A(N-1)$ zero elements in a matrix.

For example, the proposed system considers the number of Tx UCA elements $N = 8$, the number of Tx UCSA $G = 2$, and active OAM modes $L_A = 2$ out of $L = 4$. The set of AMC can be denoted as $\mathcal{L} = \{(-2,-1),(-2,1),(-1,1),(1,2)\}$. The optimal AMC is discussed in detail in Section III. Suppose active OAM mode $\mathcal{L}_3 = (-1,1)$ and index of PO state $g = 2$, that is, $f = 7$, the transmitted signal vector with the index matrix is given by

$$\begin{aligned}\boldsymbol{s} = \boldsymbol{\Lambda}_7\boldsymbol{\varsigma} &= \begin{bmatrix}0&0&0&0&0&1&0&0\\0&0&0&0&0&0&1&0\end{bmatrix}^T\begin{bmatrix}\varsigma_1\\\varsigma_2\end{bmatrix}\\ &= [\underbrace{0\quad 0\quad 0\quad 0}_{g=1}\;\underbrace{0\quad \varsigma_1\quad \varsigma_2\quad 0}_{g=2}]^T,\end{aligned} \tag{9}$$

where $\boldsymbol{\varsigma} = [\varsigma_l]_{L_A\times 1}^T$ is the active signal vector for the L_A OAM modes. Therefore, the final transmitted signal vector consists of L_A non-zero values and $(N - L_A)$ zero values.

The received signal at the mth antenna element corresponding to the lth OAM mode can be represented as

$$y_{m,l} = \sum_{l\in\mathcal{L}_k}\sum_{u=1}^{U}\frac{1}{\sqrt{U}}h_{mu}^{(g)}s_l^{(g)}e^{j\varphi_u l} + w_m = \sum_{l\in\mathcal{L}_k}h_{ml}^{(g)}s_l^{(g)} + w_m, \tag{10}$$

where w_m is the additive white Gaussian noise with zero mean and variance σ_m^2. $h_{ml}^{(g)}$ denotes the channel vector for the mth Rx UCA antenna element corresponding to the lth OAM mode, and it can be rewritten using MBF as follows:

$$\begin{aligned}h_{ml}^{(g)} &= \sum_{u=1}^{U}\frac{1}{\sqrt{U}}h_{mu}^{(g)}e^{j\varphi_u l}\\ &= \frac{A}{\sqrt{U}}\sum_{u=1}^{U}e^{j\frac{k_0 rR\cos\left(\varphi_m-\varphi_u^{(g)}\right)}{\sqrt{D^2+r^2+R^2}}}e^{j\varphi_u l}\\ &\approx \frac{A}{\sqrt{U}}e^{j(\varphi_m-\alpha_g)l}\frac{U}{2\pi}\int_0^{2\pi}e^{j\frac{k_0 rR\cos\varphi'}{\sqrt{D^2+r^2+R^2}}}e^{-j\varphi' l}\,\mathrm{d}\varphi'\\ &= A\sqrt{U}e^{j(\varphi_m-\alpha_g)l}I_l\left(\frac{k_0 rR}{\sqrt{D^2+r^2+R^2}}\right),\end{aligned} \tag{11}$$

where $A = \frac{\beta e^{-jk_0\sqrt{D^2+r_t^2+r_r^2}}}{2k_0\sqrt{D^2+r_t^2+r_r^2}}$ and $\varphi' = \varphi_m - \varphi_u^{(g)} = \varphi_m - \varphi_u - \alpha_g$. The MBF of the first kind as $I_l(x) = \frac{1}{2\pi}\int_0^{2\pi}e^{(x\cos\theta - jl\theta)}d\theta$ is used to obtain the practical impact of the OAM beam divergence corresponding to the lth mode instead of BF. In contrast to oscillatory BF solutions, MBF-based performance demonstrated that a lower-order OAM mode leads to higher capacity [22]. The MBF related to BF is represented as $I_n(x) = j^{-n}J_n(jx)$ [23].

In contrast, an OAM channel with mode properties can be represented as a matrix. The channel matrix between the gth Tx UCSA and Rx UCA $\boldsymbol{H}^{(g)}$ can be expressed as

$$\boldsymbol{H}^{(g)} = \boldsymbol{W}_{(g)}^H\boldsymbol{\Gamma}^{(g)}\boldsymbol{W}_{(g)}, \tag{12}$$

where $\boldsymbol{H}^{(g)} \in \mathbb{C}^{M\times U}$ is the circulant matrix, that is, $M = U$. $\boldsymbol{W}_{(g)} \in \mathbb{C}^{M\times M}$ is the unitary discrete Fourier transform (DFT) matrix and $\boldsymbol{\Gamma}^{(g)} \in \mathbb{C}^{M\times U}$ is a diagonal matrix, which is M-point DFT of the first row corresponding to $\boldsymbol{H}^{(g)}$. In other words, the diagonal element γ_l of $\boldsymbol{\Gamma}^{(g)}$ denotes the lth singular value corresponding to $\boldsymbol{H}^{(g)}$. Thus, the magnitudes of (11) and $\boldsymbol{\Gamma}^{(g)}$ corresponding to the lth mode are considered the channel amplitude gains and have the same value [24]. The received signal vector can be written as

$$\boldsymbol{y} = \boldsymbol{H}\boldsymbol{x} + \boldsymbol{z}, \tag{13}$$

where $\boldsymbol{H} = [\boldsymbol{H}^{(1)}\boldsymbol{H}^{(2)}\cdots\boldsymbol{H}^{(G)}]$ denotes an $M \times N$ channel matrix. At the receiver, we multiply the received vector using DFT as follows:

$$\begin{aligned}\tilde{\boldsymbol{y}} &= \boldsymbol{W}\boldsymbol{y} = \boldsymbol{W}\left(\left[\boldsymbol{H}^{(1)}\boldsymbol{x}^{(1)},\cdots,\boldsymbol{H}^{(g)}\boldsymbol{x}^{(g)},\cdots,\boldsymbol{H}^{(G)}\boldsymbol{x}^{(G)}\right]+\boldsymbol{z}\right)\\ &= \boldsymbol{\Gamma}\boldsymbol{s} + \tilde{\boldsymbol{z}}.\end{aligned} \tag{14}$$

For all possible cases of PO state, OAM mode combinations, and data symbols, the joint ML detector can be derived as follows.

$$\left(\hat{g},\hat{k}_1,\cdots,\hat{k}_{L_A},\hat{\varsigma}_{\hat{k}_1},\cdots,\hat{\varsigma}_{\hat{k}_{L_A}}\right) = \arg\min_{g,\mathcal{L}_k,\boldsymbol{s}}\|\tilde{\boldsymbol{y}} - \boldsymbol{\Gamma}\boldsymbol{s}\|^2. \tag{15}$$

where $\hat{g}$ is the active PO state, $\hat{k}_i$ is the ith active OAM mode, and $\hat{s}_{\hat{k}_i}$ is the estimated symbol value corresponding to the ith active OAM mode.

However, the ML detection method should search through all possible combinations of active OAM modes, active PO states, and modulated signals, resulting in exponentially increasing complexity as bpcu increases. To reduce the complexity of the ML detector, previous work on OAM-IM proposed a low-complexity ML detection method that utilizes the log-likelihood ratio (LLR) [12], [13]. Inspired by this, a low-complexity LLR-based ML detector is proposed for OAM-PO-IM in the next subsection.

C. PROPOSED LOW COMPLEXITY DETECTION OF OAM-PO-IM

This section introduces the proposed LLR-based low-complexity ML detection method for the OAM-PO-IM system. The proposed detection method consists of two parts. Initially, an LLR detector is employed to decode the index bits. Subsequently, an ML detector is used to decode the symbol bits. The PO state and active OAM mode combinations are identified using an LLR detector. The LLR for each OAM mode corresponding to the gth PO state can be expressed as

$$\begin{aligned}\lambda_l^{(g)} &= \ln \frac{\sum_{\varsigma\in\boldsymbol{s}} P\left(s_l=\varsigma \mid \tilde{y}_l\right)}{P\left(s_l=0 \mid \tilde{y}_l\right)} \\ &= c+\frac{|\tilde{y}_l|^2}{\sigma_n^2}+\ln\left(\sum_{\varsigma\in\boldsymbol{s}}\exp\left(-\frac{1}{\sigma_n^2}\left|\tilde{y}_l-\boldsymbol{\Gamma}^{(g)}(l,l)\varsigma\right|^2\right)\right),\end{aligned} \tag{16}$$

where c represents a constant term that can be ignored. ς denotes the modulation symbol and $\boldsymbol{\Gamma}^{(g)}(l,l)$ is the (l,l)th element of the OAM channel $\boldsymbol{\Gamma}$ corresponding to the gth PO state. The sum of the LLR for each active mode combination k corresponding to the gth PO state can be calculated as follows:

$$\lambda^{(k,g)} = \sum_{l\in\mathcal{L}_k}\lambda_l^{(g)}, \tag{17}$$

Then, the PO state $\hat{g}$ and index active mode combination $\hat{k}$ are estimated as

$$[\hat{g},\hat{k}] = \arg\max_{k,g}\lambda^{(k,g)}, \tag{18}$$

After decoding the combination of the PO state and active modes, the data symbols can be decoded via the ML detector as follows:

$$\hat{\varsigma}_l = \arg\min_{\varsigma}|\tilde{y}_l-\boldsymbol{\Gamma}^{(\hat{g})}\varsigma|^2. \tag{19}$$

III. AN EFFECTIVE AMC SELECTION SCHEME

The total capacity of an OAM system depends on predetermined index LUTs. In particular, the optimal AMC selection scheme is required to maximize the sum capacity of the OAM-IM when the number of mode combinations $p_c = 2^{\eta_L}$ and the total number of available combinations $p_a = C(L, L_A)$ are not equal $p_c \neq p_a$. With BF-based channels, the optimal AMC is not guaranteed due to the oscillatory nature of channel gain. In contrast, MBF-based models provide more stable channel gain under varying conditions. Specifically, the MBF-based model ensures a uniform beam divergence effect, where lower-order OAM modes consistently achieve higher capacity than higher-order modes. This stability facilitates a straightforward determination of the optimal AMC for the OAM-IM system. A detailed comparison of the channel gains derived from the BF and MBF models is provided in Section V.

First, the set of AMC $\mathcal{L}_{\tilde{k}}$ is sorted in descending order from the highest to the lowest sum of the channel capacity. Subsequently, the set of optimal AMC $\mathcal{L}_k$ is obtained by selecting the first p_c combinations from the sorted $\mathcal{L}_{\tilde{k}}$. Therefore, the optimal AMC $\mathcal{L}_k$ can be expressed as

$$\{\mathcal{L}_k\} = \underset{\substack{\tilde{k}=\{1,\ldots,p_a\}\\ k=\{1,\ldots,p_c\}}}{\arg\operatorname{sort}}\left(\sum_{l\in\mathcal{L}_{\tilde{k}}}\log_2\left(1+\frac{P\left|h_{ml}^{(g)}\right|^2}{\sigma_l^2 U}\right)\right). \tag{20}$$

Table 1 shows the LUTs for the proposed mode combination and conventional OAM-IM schemes, assuming a set of mode combinations of $L = 4, 6, 8$ and $L_A = 2$, with a total of $p_a = 6, 15, 28$ mode combinations and $p_c = 4, 8, 16$ possible AMC. The basic IM scheme employs initial combinations p_c and discards the remaining combinations $p_a - p_c$ (see "Conv.1" in Table 1). Otherwise, the conventional OAM-IM scheme employs LUTs to ensure a balanced selection probability for OAM modes (see "Conv.2" in Table 1) [12]. However, these schemes do not consider the property of OAM mode. According to the MBF-based channel model, the set $\mathcal{L} = [-1, 1]$ offers the highest sum capacity, whereas $\mathcal{L} = \left[\lfloor\frac{-U+1}{2}\rfloor, \cdots, \lfloor\frac{U}{2}\rfloor\right]$ has the lowest sum capacity. The proposed selection scheme is designed as a priority-based methodology, in which combinations are selected by including lower-order OAM modes within the combination. In other words, this scheme prioritizes lower-order OAM modes while intentionally reducing the use of higher-order OAM modes to mitigate the inherent problems of OAM, such as increased beam divergence. Therefore, the scheme achieves an optimized mode combination that directly contributes to improved system efficiency and markedly reduces complications associated with beam divergence. This ensures a more reliable and robust communication system, leveraging the distinct advantages of low-order OAM modes to achieve a superior performance.

IV. PERFORMANCE ANALYSIS

In this section, the upper and lower bounds of the sum capacity of the proposed system are derived using MI. Moreover, the average BER (ABER) was analyzed in the upper bound using a maximum likelihood (ML) detector under perfect CSI.

A. SUM CAPACITY ANALYSIS

According to the chain rule of MI [25], the sum capacity of OAM-PO-IM can be expressed by the MI between $\tilde{\boldsymbol{y}}$, $\boldsymbol{s}$, and f in (14), where $f = \{1, \cdots, F\}$ and $F = 2^{\eta_P+\eta_L}$, that is,

$$R(\boldsymbol{\Gamma},\boldsymbol{\Lambda}) = I(\tilde{\boldsymbol{y}};\boldsymbol{s},f) = I(\tilde{\boldsymbol{y}};\boldsymbol{s}|f)+I(\tilde{\boldsymbol{y}};f), \tag{21}$$

where $I(\tilde{\boldsymbol{y}};\boldsymbol{s}|f)$ denotes the symbol domain MI conditioned on the PO and mode combination index and is expressed using Shannon's continuous-input continuous-output memoryless

TABLE 1. Look-up table for OAM-IM with conventional and proposed mode combination schemes, $L_A = 2$.

L	p_c	scheme	$\mathcal{L}$
4	4	Conv.1	[-2 -1], [-2 1], [-2 2], [-1 1]
		Conv.2	[-2 -1], [-2 1], [-1 2], [1 2]
		Prop.	[-2 -1], [-2 1], [-1 1], [-1 2]
6	8	Conv.1	[-3 -2], [-3 -1], [-3 1], [-3 2], [-3 3], [-2 -1], [-2 1], [-2 2]
		Conv.2	[-3 3], [-2 -1], [1 2], [-3 -2], [-1 1], [2 3], [-3 -1], [-2 1]
		Prop.	[-1 1], [-1 2], [-1 -2], [1 2], [1 -2], [1 3], [-1 -3], [1 -3]
8	16	Conv.1	[-4 -3], [-4 -2], [-4 -1], [-4 1], [-4 2], [-4 3], [-4 4], [-3 -2], [-3 -1], [-3 1], [-3 2], [-3 3], [-3 4], [-2 -1], [-2 1], [-2 2]
		Conv.2	[-4 -3], [-2 -1], [1 2], [3 4], [-4 4], [-3 -2], [-1 1], [2 3], [-4 -2], [-3 -1], [1 3], [2 4], [-4 1], [-3 2], [-2 3], [-1 4]
		Prop.	[-4 -1], [-3 -1], [-2 -1], [-1 1], [-1 2], [-1 3], [-1 4], [-4 1], [-3 1], [-2 1], [1 2], [1 3], [1 4], [-3 -2], [2 3], [-2 -3]

channel's (CCMC) capacity [26] as follows:

$$I(\tilde{\mathbf{y}}; \mathbf{s}|f) = \frac{1}{F}\sum_{f=1}^{F}\log_2\left(\left|\frac{1}{\sigma_l^2}\Sigma_f\right|\right), \tag{22}$$

where $\Sigma_f = \sigma_l^2 \boldsymbol{I}_M + \frac{1}{U}\boldsymbol{\Gamma}\boldsymbol{\Lambda}_f\boldsymbol{\Lambda}_f^H\boldsymbol{\Gamma}^H$. σ_l^2 is the noise variance for the lth OAM mode. The signal-to-noise ratio (SNR) is defined as $E_s/N_o = (\lambda/(4\pi D\sigma_l))^2$, with $E_s = \mathrm{E}\left\{\|\boldsymbol{H}\boldsymbol{x}_l\|_{\mathrm{F}}^2\right\} = L_A(\lambda/(4\pi D))^2$, where E is the expectation operator and $\|\cdot\|_{\mathrm{F}}$ is the Frobenius norm [27].

The MI term for the IM domain $I(\tilde{\mathbf{y}}; f)$ represents the information transmitted by the random index switch. The closed-form lower bound for $I(\tilde{\mathbf{y}}; f)$ is given as follows [16, AppendixA]

$$I(\tilde{\mathbf{y}}; f) \geq \log_2\frac{F}{e^M} - \frac{1}{F}\sum_{f=1}^{F}\log_2\left(\sum_{t=1}^{F}\frac{|\Sigma_f|}{|\Sigma_f + \Sigma_t|}\right). \tag{23}$$

By substituting (22) and (23) into (21), a closed-form lower bound approximation can be expressed as

$$R_{\mathrm{LB}}(\boldsymbol{\Gamma}, \boldsymbol{\Lambda}) = -\frac{1}{F}\sum_{f=1}^{F}\log_2\left(\sum_{t=1}^{F}\frac{(e\sigma^2)^M/F}{|\Sigma_f + \Sigma_t|}\right). \tag{24}$$

At an asymptotically high SNR, that is, $I(\tilde{\mathbf{y}}; f) \approx \log_2 F$, the upper bound of (21) is given by

$$R_{\mathrm{UB}}(\boldsymbol{\Gamma}, \boldsymbol{\Lambda}) = \log_2 F + \frac{1}{F}\sum_{f=1}^{F}\log_2\left(\left|\frac{1}{\sigma_l^2}\Sigma_f\right|\right). \tag{25}$$

To obtain a more accurate approximation, the closed-form approximation of $R_{\mathrm{LB}}(\boldsymbol{\Gamma}, \boldsymbol{\Lambda})$ can be compensated by adding a constant gap $M(\log_2 e - 1)$ [28].

Proof: The derivations for the bounds in (24) and (25) have been validated in [16] and [28]. The tightness of the lower bound by adding a constant gap of $M(\log_2 e - 1)$ at high SNRs was demonstrated in [28]. To avoid repetition, we have omitted them for brevity. □

TABLE 2. Computational complexity comparison between OAM-IM and OAM-PO-IM.

Scheme	Detector	Real Multiplications	Complexity order
OAM-IM	ML	$(4L_A + 2L)2^{\eta_L}\mathcal{M}^{L_A}$	$2^{\eta_L}L\mathcal{M}^{L_A}$
	LLR	$7L\mathcal{M}L_A + 3L$	$LL_A\mathcal{M}$
OAM-PO-IM	ML	$(4L_A + 2L)2^{\eta_L}G\mathcal{M}^{L_A}$	$G2^{\eta_L}L\mathcal{M}^{L_A}$
	LLR	$7L\mathcal{M}L_A + G\mathcal{M}L_A + 3L$	$GLL_A\mathcal{M}$

TABLE 3. Computational complexity comparison for $L = 4$, $L_A = [1, 2, 3]$, $\mathcal{M} = 4$, and $G = [2, 3, 4]$.

Scheme	Detector	G	L_A		
			1	2	3
OAM-IM	ML	-	64 (4)	256 (6)	1024 (8)
	LLR	-	16 (4)	**32(6)**	**64(8)**
OAM-PO-IM	ML	2	128 (5)	512 (7)	2048 (9)
	LLR	2	32 (5)	64 (7)	128 (9)
		3	48 (5)	96 (7)	144 (9)
		4	**64(6)**	**128(8)**	192 (10)

B. ABER ANALYSIS WITH MAXIMUM LIKELIHOOD DETECTOR

Based on the signal model (14) and the ML detector (15), the pairwise error probability (PEP) of symbol $\boldsymbol{s}$ can be derived as

$$\begin{aligned} P(\boldsymbol{s} \to \hat{\boldsymbol{s}}) &= P\left(\|\tilde{\mathbf{y}} - \boldsymbol{\Gamma}^{(g)}\boldsymbol{s}\|^2 > \|\tilde{\mathbf{y}} - \boldsymbol{\Gamma}^{(g)}\hat{\boldsymbol{s}}\|^2\right) \\ &= Q\left(\sqrt{\frac{\left\|\boldsymbol{\Gamma}^{(g)}(\boldsymbol{s} - \hat{\boldsymbol{s}})\right\|^2}{2\sigma_n^2}}\right) \overset{(b)}{\approx} \frac{1}{12}e^{-\frac{\Delta}{4\sigma_n^2}} + \frac{1}{4}e^{-\frac{\Delta}{3\sigma_n^2}}, \end{aligned} \tag{26}$$

where (b) is used for $Q(x) \approx \frac{1}{12}e^{\frac{-x^2}{2}} + \frac{1}{4}e^{\frac{-2x^2}{3}}$ [29]. $\Delta = \left\|\boldsymbol{\Gamma}^{(g)}(\boldsymbol{s}^{(g)} - \hat{\boldsymbol{s}}^{(g)})\right\|^2$. Using (26), the upper bound of the bit

TABLE 4. Summary of simulation results with varying parameters.

no.	Performance	Summary	Varying parameters
5	Channel gain	BF vs MBF	L
6	Capacity	upper vs lower bound	L_A
7	Capacity	OAM-PO-IM vs OAM-IM vs OAM-MDM	G, N
8	Capacity	different AMC schemes	L
9	Capacity	different configuration for U and G	U, G
10	ABER	Simulation(ML,LLR) vs analytical	L_A
11	ABER	OAM-PO-IM vs OAM-IM with same bpcu	$L_A, \mathcal{M}, G$
12	ABER	different configuration for U and G	U, G
13	EE	OAM-PO-IM vs OAM-IM vs OAM-MDM	ρ

TABLE 5. Simulation parameters.

Parameter	Value
Carrier frequency, f_c	28 GHz
Wavelength, λ	0.01 m
Tx and Rx UCA radius, r_t, r_r	0.3 m
Transmission distance, D	10 m

error probability can be expressed as

$$P_b \approx \frac{1}{2^\eta} \sum_{s} \sum_{\hat{s}} \frac{P(\boldsymbol{s} \rightarrow \hat{\boldsymbol{s}}) e(\boldsymbol{s}, \hat{\boldsymbol{s}})}{\eta}, \tag{27}$$

where $e(\boldsymbol{s}, \hat{\boldsymbol{s}})$ is the number of bit errors for the corresponding pairwise error event.

C. COMPLEXITY ANALYSIS

In this section, the computational complexity of the proposed system is analyzed for the detectors and compared with that of the conventional OAM-IM system, as shown in Table 2. The complexity analysis is based on the real multiplications required for OAM-IM and OAM-MM-IM, as outlined in previous studies [12], [13]. The proposed OAM-PO-IM requires an additional detection step for the PO state compared to previous studies. According to (15), ML detection requires $(4L_A + 2L)2^{\eta_L} G\mathcal{M}^{L_A}$ real multiplications. This increase is ascribed to the index matrix $\boldsymbol{\Lambda}$, which incorporates the number of UCSA groups G, which increases the complexity compared to OAM-IM. Consequently, the computational complexity of ML detection is on the order of $\sim \mathcal{O}(G2^{\eta_L} L\mathcal{M}^{L_A})$. According to (16) to (19),, the proposed LLR-based ML detection requires $7L\mathcal{M}L_A + G\mathcal{M}L_A + 3L$, with the term $G\mathcal{M}L_A$ involving real multiplications. Therefore, the computational complexity of the LLR-based detector is on the order of $\sim \mathcal{O}(GLL_A\mathcal{M})$. Compared to OAM-IM, the complexity of OAM-PO-IM is higher when G is large for the same detector. However, when considering systems with the same bpcu, OAM-PO-IM can operate with a lower modulation order due to the additional PO index. This reduction in modulation order helps to mitigate the difference in complexity between OAM-PO-IM and OAM-IM.

For example, when $L = 4$, $L_A = [1, 2, 3]$, $\mathcal{M} = 4$, and $G = [2, 3, 4]$, the computational complexity is shown in Table 3. The OAM-PO-IM scheme exhibits a higher complexity than conventional OAM-IM when the same detectors are used. However, the LLR-based ML detector for OAM-PO-IM achieves lower complexity than the ML detector of OAM-IM, even though OAM-PO-IM transmits more bits. Furthermore, the highlighted cells in Table 3 represent cases where OAM-IM and OAM-PO-IM have the same bpcu. In this scenario, OAM-PO-IM can operate with a lower modulation order, specifically $\mathbf{M} = 2$. Although OAM-PO-IM maintains higher computational complexity compared to OAM-IM, this difference can be reduced when both systems are set up with identical bpcu.

D. ENERGY EFFICIENCY ANALYSIS

In general, energy efficiency (EE) is defined as the ratio of capacity to total system power consumption. Thus, a typical EE model is represented by

$$\eta_{\text{EE}} = \frac{BR}{\rho_{\text{tot}}}, \tag{28}$$

where B is the bandwidth, R is the capacity, ρ_{tot} is the total transmission power.

Utilizing the power consumption models of the OAM-SM, GSM and OAM-MIMO systems [15], [17], [30], the energy efficiency of the OAM-PO-IM system is analyzed and compared with those of the existing OAM-IM and OAM-MDM systems. The total transmit power for OAM-PO-IM can be expressed as

$$\rho_{\text{tot}}^{\text{POIM}} = L_A \rho_{\text{c}}^{\text{POIM}} + \delta L_A \rho + N_g \rho_{\text{sw}}, \tag{29}$$

where $\rho_{\text{c}}^{\text{POIM}}$ is the power consumed by circuits associated with an active OAM mode, δ is the slope of load-dependent power consumption, ρ is the transmit power of a transmission antenna, ρ_{sw} denotes the power consumed by a single RF switch during the UCSA group section, with $N_g = 2^{\eta_P}$ representing the number of single pole double throw (SPDT)

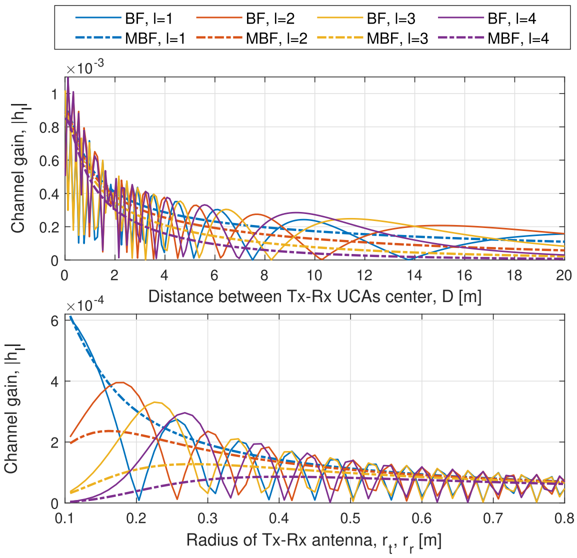

FIGURE 5. Comparison of channel gain $|h_l|$ between BF and MBF corresponding to the (a) distance between Tx-Rx UCAs center, D, (b) radius of Tx-Rx UCA, r_t, r_r, where $l = [1, 2, 3, 4]$.

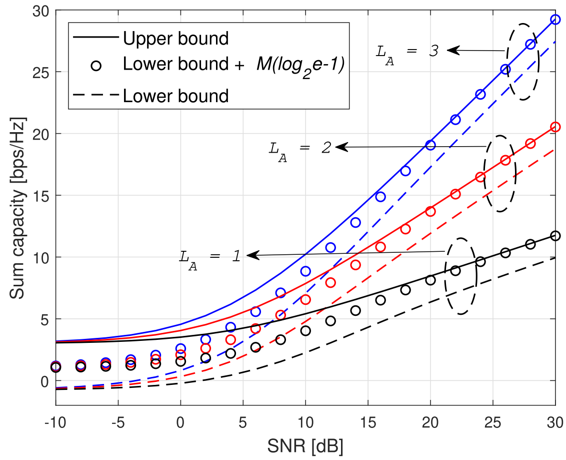

FIGURE 6. Sum capacity bound with different active modes L_A, $N = 8$, $U = 4$, $G = 2$.

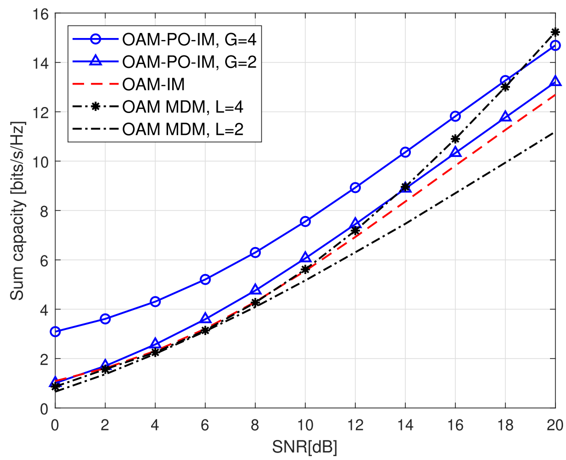

FIGURE 7. Sum capacity with different methods: OAM-PO-IM vs OAM-IM vs OAM-MDM.

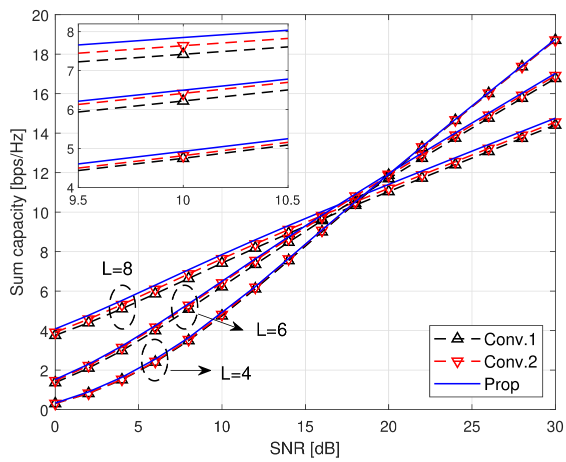

FIGURE 8. Sum capacity with different mode combination schemes, $L = \{4, 6, 8\}$, $L_A = 2$, $G = 2$.

RF switches. Each SPDT switch connects to each of the UCSA sets [31], [32]. The total circuit power consumption ρ_c^{POIM}, which includes the power of the baseband, RF chains, and low noise amplifiers (LNA), is given by [30]

$$\rho_c^{\text{POIM}} = 2\rho_{\text{BB}} + 2L\rho_{\text{RF}} + M\rho_{\text{LNA}}, \tag{30}$$

where ρ_{BB}, ρ_{RF}, and ρ_{LNA} are the power consumed by baseband processor, the RF chain of the Tx/Rx antenna, and LNA, respectively.

For existing OAM-IM and OAM-MDM systems, the total power consumption model can be represented as

$$\begin{aligned} \rho_{\text{tot}}^{\text{IM}} &= L_A\rho_c^{\text{IM}} + \delta L_A \rho, \\ \rho_{\text{tot}}^{\text{MDM}} &= L\rho_c^{\text{MDM}} + \delta L \rho, \\ \rho_c^{\text{POIM}} &= \rho_c^{\text{IM}} = \rho_c^{\text{MDM}}, \end{aligned} \tag{31}$$

Circuit power consumption is consistent across all systems since each utilizes the same number of M elements for the Rx UCA and L modes for the OAM-MDM system. However, total power requirements differ among systems. In particular, OAM-IM does not require a UCSA selection switch, while OAM-MDM demands the activation of all UCA elements.

V. RESULTS AND DISCUSSION

In this section, numerical results are presented to compare the performance of the OAM-PO-IM, OAM-IM [12], and OAM schemes, validating the analytical approach regarding the sum capacity, ABER, and energy efficiency. A summary of the simulation results for different parameters is presented in Table 4.

Table. 5 shows simulation parameters, which is considered similar to the experimental setup reported in [3] and [33]. The proposed model sets the carrier frequency to 28 GHz, corresponding to a wavelength of $\lambda = 0.01$ m. The radius of the Tx and Rx UCA is $r_t = r_r = 0.3$ m and the transmission distance is $D = 10$ m. Furthermore, the number of UCSA $G = 2, 3, 4$ and Rx UCA antenna elements $M = 4$.

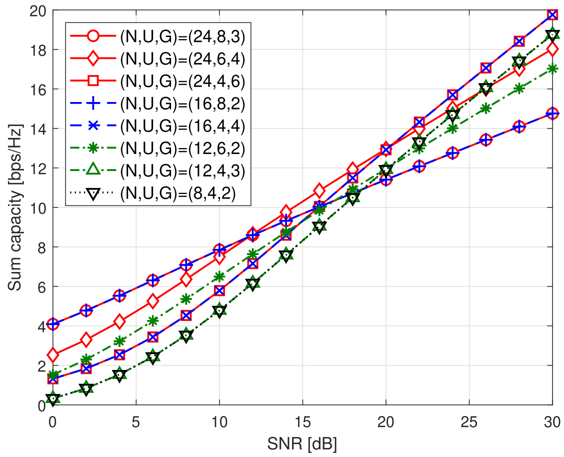

FIGURE 9. Sum capacity with different configurations for $N = 8, 12, 16, 24$, with $L_A = 2$ and $\mathcal{M} = 2$.

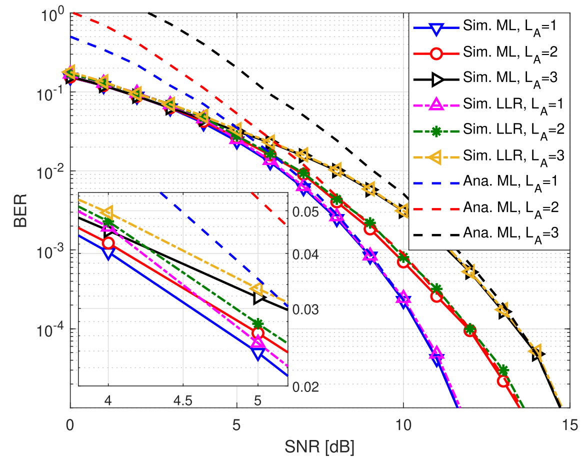

FIGURE 10. Average BER of OAM-PO-IM with different active OAM modes $L_A = 1, 2, 3$.

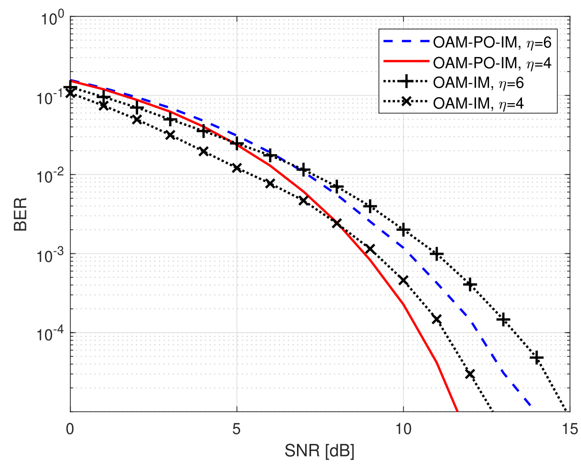

FIGURE 11. Average BER of OAM-PO-IM and OAM-IM with same bpcu, $\eta = 4, 6$.

Active modes are set as $L_A = 1, 2, 3$ among total modes L. The symbol modulation sets the binary PSK (BPSK) and the quadrature PSK (QPSK) with $\mathcal{M} = 2, 4$.

Fig. 5 shows the comparison of absolute channel gain $|h_l|$ between BF and MBF corresponding to the distance between the center of Tx-Rx UCA D and the radius of Tx-Rx UCA r_t, r_r, where $l = [1, 2, 3, 4]$. It can be observed that the BF-based channel gain for each mode oscillates as the distance and radius vary; however, the MBF-based channel gain maintains that the low-order mode achieves a better gain than the high-order mode. In conclusion, MBF- based channel modeling is a suitable approach to provide a stable basis to optimize AMC in OAM-IM systems.

A. SUM CAPACITY PERFORMANCE COMPARISON

Fig. 6 illustrates the upper and lower bounds of the sum capacity for the proposed OAM-PO-IM with varying active modes L_A. As L_A increases, both bounds increase. The lower bound with constant gap $M(\log_2 e - 1)$ and the upper bound become tighter at high SNR, that is, SNR > 25 dB. Fig. 7 compares the upper bound of the sum capacity for OAM-PO-IM, conventional OAM-IM, and OAM are indicated by solid, dashed, and dash-dotted lines, respectively. In OAM-PO-IM and OAM-IM, active modes $L_A = 2$ were selected from $L = 4$. Moreover, OAM-PO-IM varied the number of UCSA $G = 2, 4$. Due to the absence of a mode activation feature in the OAM-MDM system, we set the total number of modes $L_o = 2, 4$ to match the number of L_A and L in the IM scheme. When $L_o = L_A$, OAM-PO-IM outperformed the existing methods. When $L_o = L$, OAM-MDM performed better than OAM-PO-IM with $G = 4$ at high SNR. However, at low SNR, OAM-PO-IM demonstrates better performance than conventional techniques by approximately η_P bits as the value of G increases.

Fig. 7 presents the capacity of OAM-PO-IM with different mode combination strategies, as listed in Table 1. To compare different mode combination strategies for each identical L, at an SNR of 10 dB, the capacity gains of the proposed scheme over the conventional schemes (Conv.1 and Conv.2) are quantified as approximately 0.42 and 0.21 bps/Hz for $L = 8$, 0.28 and 0.09 bps/Hz for $L = 6$, and 0.11 and 0.04 bps/Hz for $L = 4$. This suggests that the strategy of prioritizing lower OAM modes becomes more effective in enhancing channel capacity when considering the same number of modes across the entire SNR range. To compare different L, due to the benefit of IM, a larger number of modes ($L = 8$) exhibit higher capacity when SNR < 17. However, when SNR > 17, a smaller number of modes ($L = 4$) achieve a higher capacity. This is because, as the number of modes increases, higher-order modes may be involved in active mode combinations more often than lower-order modes, which means that higher L does not always achieve higher capacity when the active mode is fixed. Therefore, it can be concluded that OAM-PO-IM is more beneficial at low SNR. However, at high SNR, the capacity remains highly dependent on the OAM-MDM scheme.

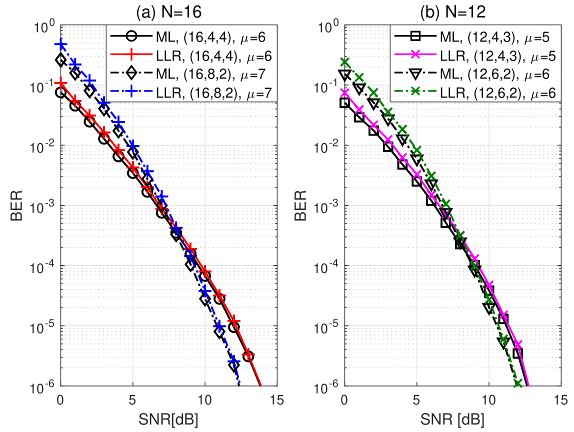

FIGURE 12. Average BER of OAM-PO-IM with different configurations (a) $N = 16$, (b) $N = 12$ with $L_A = 2$ and $\mathcal{M} = 2$.

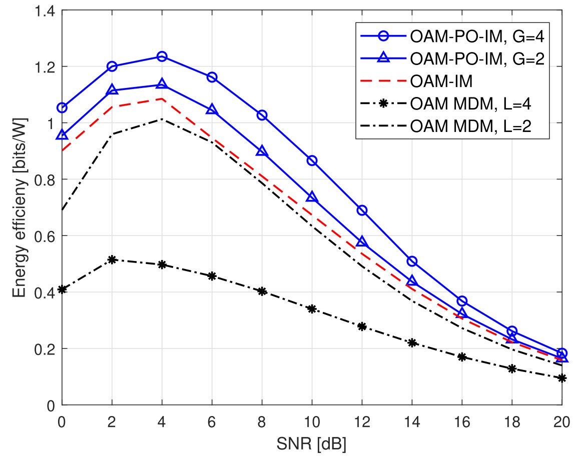

FIGURE 13. Energy efficiency with different methods: OAM-PO-IM vs OAM-IM vs OAM-MDM.

Fig. 9 illustrates the sum capacity for various configurations of the total number of Tx UCA elements $N = \{8, 12, 16, 24\}$ with fixed $L_A = 2$ and $\mathcal{M} = 2$. For a given number of N, at low SNR, a large number of UCSA elements U, which corresponds to a higher-order OAM mode $L = U$, results in a higher capacity due to the advantage of index bits. In contrast, at high SNR, the capacity for higher-order OAM mode combinations decreases due to the effects of beam divergence [11]. As the grouping parameter G increases from 2 to 4, the sum capacity across the entire SNR range also increases. However, for values of G such as 3 and 6, which are not powers of 2, the system cannot fully exploit the potential of G to enhance capacity. Instead, the capacity for these values aligns with that of the nearest lower powers of 2. In conclusion, for a given number of total elements N, a larger number of G can increase the overall capacity and mitigate the effect of beam divergence at high SNR.

B. ABER PERFORMANCE COMPARISON

Fig. 10 represents ABER for OAM-PO-IM with active modes L_A ranging from 1 to 3, and $N = 8, U = 4, G = 2$. As L_A increases, the performance of BER deteriorates. In addition, the simulated and analytical results are tighter at a high SNR for the ML detector. It can also be observed that for all values of L_A, the performance gap between the LLR and ML detectors is marginal and becomes negligible at high SNR. Therefore, the LLR detector is a viable option for practical implementation due to its significantly lower complexity.

Fig. 11 compares the ABER performance with the same bpcu $\eta = 4, 6$, where $(L_A, \mathcal{M}, G) = (1, 2, 2), (2, 2, 4)$ for the proposed OAM-PO-IM and $(L_A, \mathcal{M}) = (1, 4), (2, 4)$ for OAM-IM. To achieve the same bpcu, the OAM-IM requires a higher modulation order than the OAM-PO-IM. At low SNR regime, OAM-PO-IM exhibited a worse BER performance than OAM-IM. This is because the additional index detection for the PO state in OAM-PO-IM introduces more errors at low SNR, leading to a higher BER. However, as the SNR increases, OAM-PO-IM performs better than OAM-IM, specifically when SNR>7 for $\eta = 4$ and SNR>8 for $\eta = 6$. Notably, OAM-PO-IM shows a BER gain of approximately 0.9 dB and 1 dB at a BER of 10^{-4}.

Fig. 12 illustrates the ABER of OAM-PO-IM with different configurations for (a) $N = 16$ and (b) $N = 12$, both with fixed $L_A = 2$ and $\mathcal{M} = 2$. For Fig. 12.(a), the configurations are consistent with those of Fig. 3.(b) and (c), using $(N, U, G) = (16, 4, 4)$ and $(16, 8, 2)$, respectively. The configuration $(16, 4, 4)$, with a lower bpcu, achieves better BER performance at low SNR compared to $U = 8$. However, at high SNR, BER performance degrades due to the increased value of G in a UCA with the same radius. Fig. 12.(b) shows ABER performance for configurations $(12, 4, 3)$ and $(12, 6, 2)$. Unlike the $N = 16$ case, both configurations for $N = 12$ transmit the same PO index bit, $\mu_P = \lfloor \log_2 G \rfloor = 1$ bit, but differ in mode index bit: $\mu_L = 2$ for $(12, 4, 3)$ and $\mu_L = 3$ for $(12, 6, 2)$. Similarly to the $N = 16$ case, $(12, 4, 3)$ achieves a better BER at low SNR, but the result can be the reverse at high SNR. It can be observed that at high SNR, the configuration $(16, 4, 4)$ performs worse than others, indicating that PO state detection can lead to performance degradation compared to active mode detection. Additionally, for all configurations, the LLR detector exhibits a slight performance loss compared to the ML detector across the entire SNR range.

C. ENERGY EFFICIENCY

Fig. 13 represents the energy efficiency of OAM-PO-IM, OAM-IM, and OAM-MDM with respect to SNR ρ. The power consumption parameters were set to $\delta = 4$, $\rho_{BB} = 200$ mW, $\rho_{RF} = 250$ mW, $\rho_{LNA} = 20$ mW, and $\rho_{SW} = 5$ mW [30], [31], [32], [34]. For the sum capacity of the method, the configuration parameters were set as shown in Fig. 7, with $L = 4$ and $L_A = 2$. It can be observed that the energy efficiency of all methods increases with an increase in the SNR. When the SNR is larger than 4dB, the energy efficiency decreases with increasing SNR. When the SNR is fixed, the energy efficiency of OAM-PO-IM is larger than that of OAM-IM and OAM-MDM. Although OAM-PO-IM transmits extra bits and uses more power because of the PO state, the power increase is less significant compared to the capacity boost gained from antenna switching, leading to enhanced energy efficiency.

VI. CONCLUSION

In this paper, a novel OAM-IM was introduced and analyzed by employing PO states of misalignment in UCA-based OAM communication. The PO state according to UCSA selection does not affect the distortion of OAM mode orthogonality but can be a distinguishing index information using different phase profiles. Furthermore, MBF was applied to derive a channel model to obtain an effective AMC. Traditional ML and a new low-complexity LLR-based ML detector were proposed and compared with existing OAM-IM. The simulation results showed that the proposed scheme can provide better sum capacity with the equivalent system configuration and better BER performance compared to conventional OAM-IM under the same bpcu conditions at high SNR region.

In the future, this study can be extended to analyze non-LoS scenarios and tilt/displacement misalignment, which present challenges in detecting index bits in practical OAM communication systems. Addressing these challenges would require more sophisticated channel modeling, beam steering, and robust detection schemes [6], [18], [35]. Additionally, a new mode combination method can be investigated to include the mode 0 state, potentially improving capacity. Second, replacing a single UCA with multiple concentric UCAs may increase the system's multiplexing gain [11], [33]. Future research could focus on optimizing UCSA configurations across multiple UCAs and selecting the optimal placement of active elements to maximize sum capacity. Lastly, conducting experimental validation is a critical area for future research to verify the proposed models in real-world scenarios.

REFERENCES

[1] R. Chen, H. Zhou, M. Moretti, X. Wang, and J. Li, "Orbital angular momentum waves: Generation, detection, and emerging applications," *IEEE Commun. Surveys Tuts.*, vol. 22, no. 2, pp. 840–868, 2nd Quart., 2020.

[2] O. Edfors and A. J. Johansson, "Is orbital angular momentum (OAM) based radio communication an unexploited area?" *IEEE Trans. Antennas Propag.*, vol. 60, no. 2, pp. 1126–1131, Feb. 2012.

[3] Y. Yagi, H. Sasaki, T. Yamada, and D. Lee, "200 Gb/s wireless transmission using dual-polarized OAM-MIMO multiplexing with uniform circular array on 28 GHz band," *IEEE Antennas Wireless Propag. Lett.*, vol. 20, pp. 833–837, 2021.

[4] M. I. W. Khan, J. Woo, X. Yi, M. I. Ibrahim, R. T. Yazicigil, A. P. Chandrakasan, and R. Han, "A 0.31-THz orbital-angular-momentum (OAM) wave transceiver in CMOS with bits-to-OAM mode mapping," *IEEE J. Solid-State Circuits*, vol. 57, no. 5, pp. 1344–1357, May 2022.

[5] H. Yang, S. Zheng, H. Zhang, N. Li, D. Shen, T. He, Z. Yang, Z. Lyu, and X. Yu, "A THz-OAM wireless communication system based on transmissive metasurface," *IEEE Trans. Antennas Propag.*, vol. 71, no. 5, pp. 4194–4203, May 2023.

[6] R. Chen, W.-X. Long, X. Wang, and L. Jiandong, "Multi-mode OAM radio waves: Generation, angle of arrival estimation and reception with UCAs," *IEEE Trans. Wireless Commun.*, vol. 19, no. 10, pp. 6932–6947, Oct. 2020.

[7] W. Cheng, W. Zhang, H. Jing, S. Gao, and H. Zhang, "Orbital angular momentum for wireless communications," *IEEE Wireless Commun.*, vol. 26, no. 1, pp. 100–107, Feb. 2019.

[8] R. Chen, H. Xu, M. Moretti, and J. Li, "Beam steering for the misalignment in UCA-based OAM communication systems," *IEEE Wireless Commun. Lett.*, vol. 7, no. 4, pp. 582–585, Aug. 2018.

[9] M. Jian, Y. Chen, and G. Yu, "Non-coaxial OAM: Precoding design, misaligned parameter estimation and capacity compensation," *IEEE Access*, vol. 9, pp. 37726–37738, 2021.

[10] S. M. Mohammadi, L. K. S. Daldorff, J. E. S. Bergman, R. L. Karlsson, B. Thide, K. Forozesh, T. D. Carozzi, and B. Isham, "Orbital angular momentum in radio—A system study," *IEEE Trans. Antennas Propag.*, vol. 58, no. 2, pp. 565–572, Feb. 2010.

[11] H. Jing, W. Cheng, Z. Li, and H. Zhang, "Concentric UCAs based low-order OAM for high capacity in radio vortex wireless communications," *J. Commun. Inf. Netw.*, vol. 3, no. 4, pp. 85–100, Dec. 2018.

[12] E. Basar, "Orbital angular momentum with index modulation," *IEEE Trans. Wireless Commun.*, vol. 17, no. 3, pp. 2029–2037, Mar. 2018.

[13] V. Vahidinia, M. Atashbar, and S. Hosseinzadeh, "Orbital angular momentum and mode multiplexing based index modulation," *Phys. Commun.*, vol. 48, Oct. 2021, Art. no. 101407.

[14] M. Chen, R. Chen, Y. Zhao, Z. Yang, and Y. L. Guan, "Index-modulation OAM detectors resistant to beam misalignment," *IEEE Trans. Veh. Technol.*, vol. 73, no. 2, pp. 2836–2841, Feb. 2024.

[15] X. Ge, R. Zi, X. Xiong, Q. Li, and L. Wang, "Millimeter wave communications with OAM-SM scheme for future mobile networks," *IEEE J. Sel. Areas Commun.*, vol. 35, no. 9, pp. 2163–2177, Sep. 2017.

[16] L. He, J. Wang, and J. Song, "On generalized spatial modulation aided millimeter wave MIMO: Spectral efficiency analysis and hybrid precoder design," *IEEE Trans. Wireless Commun.*, vol. 16, no. 11, pp. 7658–7671, Nov. 2017.

[17] W. Qu, M. Zhang, X. Cheng, and P. Ju, "Generalized spatial modulation with transmit antenna grouping for massive MIMO," *IEEE Access*, vol. 5, pp. 26798–26807, 2017.

[18] L. Liang, W. Cheng, W. Zhang, and H. Zhang, "Joint OAM multiplexing and OFDM in sparse multipath environments," *IEEE Trans. Veh. Technol.*, vol. 69, no. 4, pp. 3864–3878, Apr. 2020.

[19] H. Jing, W. Cheng, X.-G. Xia, and H. Zhang, "Orbital-angular-momentum versus MIMO: Orthogonality, degree of freedom, and capacity," in *Proc. IEEE 29th Annu. Int. Symp. Pers., Indoor Mobile Radio Commun. (PIMRC)*, Sep. 2018, pp. 1–7.

[20] M. Xie, X. Gao, M. Zhao, W. Zhai, W. Xu, J. Qian, M. Lei, and S. Huang, "Mode measurement of a dual-mode radio frequency orbital angular momentum beam by circular phase gradient method," *IEEE Antennas Wireless Propag. Lett.*, vol. 16, pp. 1143–1146, 2017.

[21] M. H. Lee, H. Y. Lee, and S. Y. Shin, "Divergence intensity and mode combinations for multiple orbital angular momentum transmission," *ICT Exp.*, vol. 9, no. 6, pp. 1053–1058, Dec. 2022.

[22] Z. Zhang, Y. Yuan, J. Cang, H. Wu, and X. Zhang, "An orbital angular momentum-based in-band full-duplex communication system and its mode selection," *IEEE Commun. Lett.*, vol. 21, no. 5, pp. 1183–1186, May 2017.

[23] M. Abramowitz and I. A. Stegun, *Handbook of Mathematical Functions With Formulas, Graphs, and Mathematical Tables*, vol. 55. Washington, DC, USA: U.S. Government Printing Office, 1964.

[24] H. Jing, W. Cheng, W. Zhang, and H. Zhang, "Optimal UCA design for OAM based wireless backhaul transmission," in *Proc. IEEE Int. Conf. Commun. (ICC)*, Jun. 2020, pp. 1–6.

[25] M. Thomas and A. T. Joy, *Elements of Information Theory*. Hoboken, NJ, USA: Wiley-Interscience, 2006.

[26] O. E. Ayach, S. Rajagopal, S. Abu-Surra, Z. Pi, and R. W. Heath, "Spatially sparse precoding in millimeter wave MIMO systems," *IEEE Trans. Wireless Commun.*, vol. 13, no. 3, pp. 1499–1513, Mar. 2014.

[27] R. Mesleh and A. Younis, "Capacity analysis for LOS millimeter–wave quadrature spatial modulation," *Wireless Netw.*, vol. 24, no. 6, pp. 1905–1914, Aug. 2018.

[28] L. He, J. Wang, and J. Song, "Spatial modulation for more spatial multiplexing: RF-chain-limited generalized spatial modulation aided MM-wave MIMO with hybrid precoding," *IEEE Trans. Commun.*, vol. 66, no. 3, pp. 986–998, Mar. 2018.

[29] M. Chiani and D. Dardari, "Improved exponential bounds and approximation for the Q-function with application to average error probability computation," in *Proc. Global Telecommun. Conf. (GLOBECOM)*, vol. 2, 2002, pp. 1399–1402.
[30] R. Chen, H. Zhou, W.-X. Long, and M. Moretti, "Spectral and energy efficiency of line-of-sight OAM-MIMO communication systems," *China Commun.*, vol. 17, no. 9, pp. 119–127, Sep. 2020.
[31] R. Mesleh and A. Alhassi, *Space Modulation Techniques*. Hoboken, NJ, USA: Wiley, 2018.
[32] R. Méndez-Rial, C. Rusu, N. González-Prelcic, A. Alkhateeb, and R. W. Heath, "Hybrid MIMO architectures for millimeter wave communications: Phase shifters or switches?" *IEEE Access*, vol. 4, pp. 247–267, 2016.
[33] H. Sasaki, Y. Yagi, H. Fukumoto, and D. Lee, "OAM-MIMO multiplexing transmission system for high-capacity wireless communications on millimeter-wave band," *IEEE Trans. Wireless Commun.*, vol. 23, no. 5, pp. 3990–4003, May 2024.
[34] G. Auer, V. Giannini, I. Gódor, P. Skillermark, M. Olsson, M. A. Imran, D. Sabella, M. J. Gonzalez, C. Desset, and O. Blume, "Cellular energy efficiency evaluation framework," in *Proc. IEEE 73rd Veh. Technol. Conf. (VTC Spring)*, 2011, pp. 1–6.
[35] M. Jian, "NLOS OAM-MIMO transmission: Misaligned channel analysis and pre-processing scheme design," in *Proc. Int. Wireless Commun. Mobile Comput. (IWCMC)*, 2020, pp. 1866–1871.

HYE YEONG LEE received the B.S. degree in electrical engineering and the M.S. and Ph.D. degrees in IT convergence engineering from the Kumoh National Institute of Technology (KIT), South Korea, in 2016, 2018, and 2022, respectively. She is currently a Postdoctoral Fellow and a Researcher with ICT-CRC, KIT. Her research interests include 5G/6G wireless communications and networks, signal processing, non-orthogonal multiple access (NOMA), multiple-input multiple-output (MIMO) antenna, index modulation (IM), and orbital angular momentum (OAM).

MAN HEE LEE (Member, IEEE) received the B.S. degree in electrical engineering and the M.S. and Ph.D. degrees from the Department of IT Convergence Engineering, Kumoh National Institute of Technology (KIT), Gumi, South Korea, in 2016, 2018, and 2024, respectively. From 2018 to 2020, he was a DSP/FW Engineer at the company. Currently, he is a Postdoctoral Fellow with the Wireless and Emerging Network System (WENS) Laboratory, Department of IT Convergence Engineering, KIT. His main research interests include future radio access (FRA) for next generation networks, non-orthogonal multiple access (NOMA), orbital angular momentum (OAM), MIMO, and DSP.

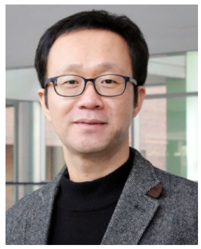

SOO YOUNG SHIN (Senior Member, IEEE) received the B.S., M.S., and Ph.D. degrees in electrical engineering and computer science from Seoul National University, South Korea, in 1999, 2001, and 2006, respectively. He was a Visiting Scholar with the FUN Laboratory, University of Washington, USA, from July 2006 to June 2007. After three years working with the WiMAX Design Laboratory, Samsung Electronics, he has been an Associate Professor with the School of Electronics, Kumoh National Institute of Technology, since September 2010. His research interests include wireless LAN, WPAN, WBAN, wireless mesh networks, sensor networks, coexistence among wireless networks, industrial and military networks, cognitive radio networks, and next-generation mobile wireless broadband networks.